Generation of localized patterns in anharmonic lattices with cubic-quintic nonlinearities and fourth-order dispersion via a variational approach

Etienne Wamba[1,2,3,*] and Aurélien S. Tchakoutio Nguetcho[4,5]

[1]*State Research Center OPTIMAS, and Fachbereich Physik, Technische Universität Kaiserslautern, D-67663 Kaiserslautern, Germany*

[2]*African Institute for Mathematical Sciences, P.O. Box 608, Limbe, Cameroon*

[3]*Abdus Salam International Centre for Theoretical Physics, P.O. Box 586, I-34014, Trieste, Italy*

[4]*Laboratoire LISSAS, Département de Physique, Faculté des Sciences, Université de Maroua, B.P. 814, Maroua, Cameroun*

[5]*Laboratoire LE2I, Université de Bourgogne Franche-Comté, B.P. 47870, F-21078, Dijon, France*

(Received 12 February 2018; published 14 May 2018)

We use the time-dependent variational method to examine the formation of localized patterns in dynamically unstable anharmonic lattices with cubic-quintic nonlinearities and fourth-order dispersion. The governing equation is an extended nonlinear Schrödinger equation known for modified Frankel-Kontorova models of atomic lattices and here derived from an extended Bose-Hubbard model of bosonic lattices with local three-body interactions. In presence of modulated waves, we derive and investigate the ordinary differential equations for the time evolution of the amplitude and phase of dynamical perturbation. Through an effective potential, we find the modulationally unstable domains of the lattice and discuss the effect of the fourth-order dispersion in the dynamics. Direct numerical simulations are performed to support our analytical results, and a good agreement is found. Various types of localized patterns, including breathers and solitonic chirped-like pulses, form in the system as a result of interplay between the cubic-quintic nonlinearities and the second- and fourth-order dispersions.

DOI: 10.1103/PhysRevE.97.052207

I. INTRODUCTION

The required beauty of good physical models resides in both their simplicity and universality. Although universal models are useful in describing a variety of different phenomena, they are rarely available in physics in spite of their key importance. Examples of such models are the Bose-Hubbard (BH) model [1] and the Frenkel-Kontorova (FK) model [2], which are interesting in condensed matter physics.

The BH model is a simple model that captures the relevant features of boson physics in a variety of physical systems which are analogs of interacting spinless bosons in a lattice. The key ingredients of the dynamics of BH systems include the hopping of the particles between lattice sites and the interaction between the particles, which correspond to kinetic and potential energies, respectively. Such a model has become very famous [3–6] in the quantum gas field as it describes the basic physics of bosonic atoms in an optical lattice and can be experimentally achieved and manipulated [7]. For instance, in an experiment on the transport of ultracold atoms trapped in an optical lattice, it has been shown that phase slips can lead to dissipation in a clean and well-characterized Bose-Hubbard system [5]. It has also been obtained that moderate interactions induce dynamical thermalization in a Bose-Hubbard ring of finite size with disorder containing a finite number of bosons [6]. The BH model may also describe the physics of open quantum systems [5,8,9].

As for the FK model, it has become very popular in many niches of solid state and nonlinear physics [2,10–14]. The standard FK model describes a (one-dimensional) chain of atoms coupled to each other and sitting on a periodic substrate (on-site) potential. In the Hamiltonian that describes the chain, the potential energy consists of two contributions: the substrate external potential present along the chain and the potential due to general interparticle interactions. The substrate potential was initially taken to be of sinusoidal form, although more elaborate forms are known today. This traditional model has some basic restrictions, which makes it applicable for small lattice misfits only. It uses the purely elastic interaction between neighboring atoms as a substitute for the real interatomic forces. In addition, the shape of the substrate potential in real physical systems can deviate from the standard (sinusoidal or rigid) one, and this may affect strongly the transport properties of the system.

FK models [15] as well as BH models [16,17] have proven capable of supporting the generation and propagation of solitons through the process of modulational (or dynamical) instability. Such a process consists in a spontaneous growth of sidebands of a continuous- or plane-wave train in a nonlinear dispersive medium [18]. This phenomenon is of common occurrence in nonlinear wave propagation through plasmas, fluids, cold gases, and condensed matter [19,20]. The early stage of the evolution of the modulationally unstable modes is marked in general with an exponential growth in the wave amplitude. In optical systems, such an amplification is done at the expense of the pumping mode, up to some distance where the saturation of the growth rate occurs owing to pump depletion [19]. The subsequent wave dynamics may exhibit a recurrent or quasiperiodic exchange of energy between infinitely many spectral modes, which leads to the formation of localized patterns in the system [21]. Solitons and modulational

*Corresponding author: wamba.etienne@gmail.com

instability are inherently linked, the latter being the underlying physical mechanism that creates such localized nonlinear waves.

Localized patterns are generated not only with simple models, but also with elaborate ones which are closer to real systems where the patterns naturally occur. As a better approach for modeling real systems, several extensions of the standard BH and FK models have been introduced. For the BH model, the modifications include, for instance, the Bogoliubov back-reaction approximation, which is a higher-order mean field theory, formulated by considering additional contributions for the normal and anomalous density operators [4]. The standard BH model has also been extended by including a two-body interaction between nearest-neighboring sites [22] or an on-site three-body interaction [23,24]. As for the FK model, the improvement has been achieved either by introducing a variety of external periodic potentials [2], or by modifying the atom-atom interaction potential, or both types of potentials [14,15,25,26]. Though in most investigated FK models the nonlinearity often comes from an on-site potential [27,28], it has been shown that interactions between particles may be anharmonic [2,14], leading to more realistic models.

Thereby, in a recent work we considered the lattices with several higher-order anharmonicities and introduced a new modified FK model that led us to an extended nonlinear Schrödinger (eNLS) equation including cubic-quintic nonlinearities as well as second- and fourth-order dispersions. Then we looked at the coupled effects of deformability and nonlinearity on the modulational instability of anharmonic deformable atomic lattices, and the nonlinear excitations were studied using the linear stability analysis. The eNLS equation has also been examined with linear stability analysis in the context of optical waves [29]. However, despite the nice results obtained via the linear stability method in those studies, that employed technique did not allow studying and describing the dynamics beyond the instability onset point. In this work, we briefly revisit the above eNLS equation for an anharmonic chain of atoms and derive a similar equation for a BH lattice with three-body interaction in the limit of long wavelengths. We aim at answering that unresolved issue not only for the optical waves and the FK model, but also for the BH lattice. For this, we reconsider the dynamical instability of the system via the time-dependent variational approach (TDVA) and numerical calculations. The TDVA reveals further dynamical features of the system that cannot be resolved through the linear stability analysis.

The paper is structured as follows: in Sec. II we present the theoretical model that describes both the displacement of particles in a deformable lattice in the limit of small-amplitude oscillations and the evolution of a Bose-Hubbard lattice with three-body interaction in the limit of long wavelengths. Section III is devoted to the analytical framework in which we derive not only the instability conditions of the model, but also the evolution equations for the perturbation using the time-dependent variational approach. By solving the equations, the dynamics of the system is studied in both cases of focusing and defocusing nonlinearity. Then in Sec. IV we perform direct numerical integrations to check the validity of the predictions found by analytical methods and study the interplay between the effective nonlinearity and the effective dispersion. Localized structures are generated in the lattice for modes chosen in safe parameter domains. Section V summarizes our results and concludes the work.

II. THE GOVERNING MODEL

In order to derive the equation sought for, we may start from two models, namely, the nonlinear Klein-Gordon equation or the extended BH model, yet different, but yielding the same behavior.

A. Lattice model based on the nonlinear Klein-Gordon equation

The continuum analog of the standard FK model is the integrable sine-Gordon equation, while its generalization is the so-called nonlinear Klein-Gordon equation. It can describe a one-dimensional chain of atoms that are coupled harmonically to their nearest neighbors and subjected to an external on-site potential. Let θ_n be the displacement of the nth atom. The motion for low-amplitude oscillations can be described using a lattice model based on the following nonlinear Klein-Gordon equation with an on-site potential of deformable shape [10]:

$$\frac{d^2\theta_n}{d\tau^2} = P_2(\theta_{n+1} + \theta_{n-1} - 2\theta_n) - \omega_0'^2\left(\theta_n + \varepsilon^2\beta\,\theta_n^3 + \varepsilon^4\eta\,\theta_n^5\right). \quad (1)$$

The parameter P_2 is the characteristic velocity of the lattice, ω_0' is a function of the characteristic frequency ω_0 of the lattice, and $\epsilon \ll 1$ is the smallness parameter. We get the coefficients in the right-hand side of Eq. (1) by Taylor-expanding a relevant substrate potential, which we choose to be the Peyrard-Remoissenet potential [10] known for its symmetry and deformability properties. It can be seen that the terms in $\varepsilon^i (i = 1,3)$ are absent. We get $\omega_0' = \sqrt{2}\omega_0/2\sigma$ and $\beta(\sigma) = (2\sigma^2 - 3)/6\sigma^2$ and $\eta(\sigma) = (17\sigma^4 - 60\sigma^2 + 45)/240\sigma^4$ because odd terms in the expansion vanish. Interestingly, the two last parameters are functions of the shape parameter σ of the external potential and can be positive or negative, which makes broader the scope of the work.

By means of the multiple-scale method combined with the semidiscreteness approximation introduced by Tsurui [30], it is possible to reveal the effects of anharmonicity and discreteness of the system. For this, we set

$$\theta_n(\tau) = \psi(x,t)e^{i\phi_n} + \text{c.c.}, \quad (2)$$

where c.c. denotes the complex conjugate and $i = \sqrt{-1}$. The so-called "fast" variable $\phi_n = Kn - \omega\tau$, representing the phase of the carrier wave, is taken to be completely discrete. The multiple-scale variables x and t, defined by $x = \varepsilon(n - v_g\tau)$ and $\tau = t$, respectively, are called "slow" variables. $v_g \equiv d\omega/dK$ is the group velocity associated to the wave packet. The wave number K and the frequency of the carrier wave ω satisfy the lattice linear dispersion relation

$$\omega^2 = \omega_0'^2 + 4P_2\sin^2(K/2). \quad (3)$$

In what follows, we restrict our analysis to systems near the lower gap ($K = 0$) where v_g is zero. Combining Eqs. (2) and (1), it is found that the envelope part of the scalar dimensionless displacement of the nth particle in the lattice obeys a nonlinear

Schrödinger equation in the form

$$\mathrm{i}\frac{\partial\psi}{\partial t}+P_1\frac{\partial^2\psi}{\partial x^2}-G_1|\psi|^2\psi-G_2|\psi|^4\psi=-\frac{P_2}{24\omega}\frac{\partial^4\psi}{\partial x^4}, \quad (4)$$

with the group-velocity dispersion coefficient $P_1=P_2/2\omega$. G_1 and G_2 are the nonlinear coefficients and are related to the shape parameter σ by $G_1(\sigma)=-(3-2\sigma^2)\omega_0/8\sigma^4$, $G_2=-(17\sigma^4-60\sigma^2+45)\omega_0/96\sigma^6$ near the lower gap edge, i.e., the edge where $K=0$ and $\omega=\sqrt{2}\omega_0/2\sigma$. Although P_2 is related to P_1, for the sake of generality, we are investigating in what follows the case where P_2 is arbitrary before considering the particular case $P_2=2\omega P_1$. We take P_2 to be in units of 24ω. Hence, in the limit of small-amplitude oscillations, the envelope ψ satisfies the eNLS equation:

$$\mathrm{i}\,\psi_t=-P_1\,\psi_{xx}-P_2\,\psi_{xxxx}+G_1\,|\psi|^2\psi+G_2\,|\psi|^4\psi, \quad (5)$$

where P_1 and P_2 are the second- and fourth-order dispersion parameters, respectively. The cubic and quintic nonlinearity strengths G_1 and G_2, respectively, can be taken as positive or negative. In most computations, Eq. (5) is going to be used as the governing equation. A similar equation may also be obtained for a modified BH model.

B. Bose-Hubbard lattice with local three-body interaction

We consider a cold gas of bosonic atoms with local (on-site) two- and three-body interactions, trapped in a one-dimensional optical lattice and confined to the lowest Bloch band. The simplest model that governs the dynamics of the system is the Bose-Hubbard Hamiltonian. On a chain with ℓ lattice sites (with open boundary conditions), the Hamiltonian reads [23,24]

$$\hat{H}=-J\sum_{i=1}^{\ell-1}(\hat{b}_i^\dagger\hat{b}_{i+1}+\mathrm{H.c.})+\frac{1}{2!}U\sum_{i=1}^{\ell}\hat{n}_i(\hat{n}_i-1)+\frac{1}{3!}W\sum_{i=1}^{\ell}\hat{n}_i(\hat{n}_i-1)(\hat{n}_i-2), \quad (6)$$

where $\hat{b}_i$ and $\hat{b}_i^\dagger$ are annihilation and creation field-operators, respectively, for a particle in site i, and $\hat{n}_i=\hat{b}_i^\dagger\hat{b}_i$ is the local particle number operator; H.c. denotes the Hermitian conjugate. We have considered only on-site two- and three-body interactions, with strengths U and W, respectively, and nearest-neighbor tunneling, with hopping rate J. These approximations rely on the fact that adjacent site interactions and next-to-nearest-neighbor tunneling amplitudes are generally at least two orders of magnitude smaller than on-site interactions and nearest-neighbor hopping [4]. Moreover, the model assumes that the finite three-body repulsion ($W>0$) is still sufficiently large to prevent an attractive system ($U<0$) from collapsing [24]. Even though the three-body losses dominate in the system, they occur in a gradual (not instantaneous) way. One may readily show that the above equation can be rewritten without $\hat{n}$ as

$$\hat{H}=-J\sum_i(\hat{b}_i^\dagger\hat{b}_{i+1}+\hat{b}_{i+1}^\dagger\hat{b}_i)+\frac{U}{2}\sum_i\hat{b}_i^\dagger\hat{b}_i^\dagger\hat{b}_i\hat{b}_i+\frac{W}{6}\sum_i\hat{b}_i^\dagger\hat{b}_i^\dagger\hat{b}_i^\dagger\hat{b}_i\hat{b}_i\hat{b}_i. \quad (7)$$

Using the Hamiltonian in Eq. (7) we can easily write the Heisenberg equations of motion for the field operators $\hat{b}_i$, i.e., $\mathrm{i}\dot{\hat{b}}_i=[\hat{b}_i,\hat{H}]$. After a straightforward calculation, we obtain

$$\mathrm{i}\partial_t\hat{b}_i=-J(\hat{b}_{i-1}+\hat{b}_{i+1})+\tilde{G}_1\hat{n}_i\hat{b}_i+\tilde{G}_2\hat{n}_i^2\hat{b}_i, \quad (8)$$

where $\tilde{G}_1=U-W/2$ and $\tilde{G}_2=W/2$. Assume we deal with coherent many-body states with a well-defined phase between the lattice sites. Then we can derive the lowest-order mean-field theory for the Bose-Hubbard model by replacing in the above Heisenberg (8) the field operators $\hat{b}_i$ and $\hat{b}_i^\dagger$ by the c-number fields b_i and b_i^*, respectively. We obtain the discrete mean-field equation

$$\mathrm{i}\partial_t b_i=-J(b_{i-1}+b_{i+1})+\tilde{G}_1|b_i|^2b_i+\tilde{G}_2|b_i|^4b_i. \quad (9)$$

The mean-field equation readily leads to the discrete Gross-Pitaevskii equation when we rescale the field and time as $b_i\to\sqrt{N}b_i$ and $t\to 2Jt$, where N is the atom number. In that case, the effective two- and three-body interactions strengths rescale as $\tilde{G}_1\to\tilde{G}_1N/2J$ and $\tilde{G}_2\to\tilde{G}_2N^2/2J$. In the long-wavelength limit, we may set $b_i(t)=\phi(x,t)$ and $x=i\kappa$, and then $b_{i\mp1}(t)=\phi(x\mp\kappa,t)$, where κ is the lattice constant. Next, we Taylor expand $\phi(x\mp\kappa,t)$ to the fourth order in x and replace in Eq. (9). Then taking $\phi(x,t)=\tilde{\psi}(x,t)\exp(2\mathrm{i}Jt)$ into the resultant equation yields the equation

$$\mathrm{i}\tilde{\psi}_t=-\tilde{P}_1\tilde{\psi}_{xx}-\tilde{P}_2\tilde{\psi}_{xxxx}+\tilde{G}_1|\tilde{\psi}|^2\tilde{\psi}+\tilde{G}_2|\tilde{\psi}|^4\tilde{\psi}, \quad (10)$$

where $\tilde{P}_1=J\kappa^2$ and $\tilde{P}_2=J\kappa^4/12$. We clearly see that Eq. (10), which has just been derived from an extended BH model in the long-wavelength limit, and Eq. (5), which is known for a modified FK model in the small-amplitude limit or for optical waves, do have exactly the same form. If in particular we set $\tilde{\omega}=\kappa^2/24$, then we have the constraint $\tilde{P}_2=2\tilde{\omega}\tilde{P}_1$ obtained in the case of atomic lattices. Hence, the Bose-Hubbard model in the presence of on-site three-body interaction can lead to an eNLS equation with cubic-quintic nonlinearities and second- and fourth-order dispersions in the limit of long wavelengths. We are going to apply the TDVA technique to analytically examine the equation.

III. ANALYTICAL RESULTS

A. Evolution equation for the modulational perturbation: The variational method

The variational technique is known to be a very useful tool in the investigation of dynamical properties of various systems in physics and many other sciences. Here we use a variant called the time-dependent variational approach to examine the dynamical instability (DI) of the theoretical model of the lattice described above. In this well-known variant [31,32], the first step of the process consists in finding the Lagrangian density that may generate the governing Eq. (5). We find that such a density is given by

$$\mathcal{L}=\frac{\mathrm{i}}{2}(\psi^*\partial_t\psi-\mathrm{c.c.})-P_1|\nabla_x\psi|^2+P_2\left|\nabla_x^2\psi\right|^2-\frac{G_1}{2}|\psi|^4-\frac{G_2}{3}|\psi|^6, \quad (11)$$

where c.c. denotes the complex conjugate. We use a DI-motivated variational ansatz for the wave function in the form

$$\psi(x,t) = \left(\psi_0 + \sqrt{\frac{a(t)}{2}}e^{i[qx+\frac{b(t)}{2}]} + \sqrt{\frac{a(t)}{2}}e^{-i[qx-\frac{b(t)}{2}]}\right) \times \exp[\mathrm{i}(kx-\Omega t)], \tag{12}$$

where $\Omega = P_1k^2 - P_2k^4 + G_1\psi_0^2 + G_2\psi_0^4$ is the linear dispersion relation of the system.

The traditional technique requires to substitute this trial wave function into the Lagrangian density which may be integrated over the entire space to obtain the effective Lagrangian. However, there exists a tricky way of computing the effective Lagrangian for this type of problem. It consists in considering rather an annular one-dimensional geometry, which imposes periodic boundary conditions on the wave function $\psi(x,t)$ and integration limits $0 \leqslant x < 2\pi$. This causes the quantization of the wave numbers, i.e., $k,q = 0, \pm 1, \pm 2, \pm 3, \ldots$. In this defined geometry, calculating the effective Lagrangian yields

$$\begin{aligned} L_{\mathrm{eff}} = -\pi\big[&\tfrac{5}{3}G_2a^3 + a^2\big(6G_2\psi_0^2\cos b + 9G_2\psi_0^2 + \tfrac{3}{2}G_1\big) \\ &+ a\big(\dot{b} + 4G_2\psi_0^4\cos b + 2G_1\psi_0^2\cos b + 4G_2\psi_0^4 \\ &+ 2G_1\psi_0^2 - 12P_2k^2q^2 - 2P_2q^4 + 2P_1q^2\big) \\ &- \tfrac{4}{3}G_2\psi_0^6 - G_1\psi_0^4\big]. \end{aligned} \tag{13}$$

The dot in the above equation stands for the derivative with respect to time. With the variational effective Lagrangian L_{eff}, it is possible to derive the evolution equations for the time-dependent variational parameters introduced in Eq. (12). For this, we use the corresponding Euler-Lagrange equations based on L_{eff}. In the generalized form, these equations are

$$\frac{\mathrm{d}}{\mathrm{d}t}\left(\frac{\partial L_{\mathrm{eff}}}{\partial\dot{\xi}_i}\right) - \frac{\partial L_{\mathrm{eff}}}{\partial\xi_i} = 0, \tag{14}$$

where ξ_i and $\dot{\xi}_i$ represent, respectively, the generalized coordinate and corresponding generalized velocity. Plugging the effective Lagrangian into that equation, we obtain the following coupled set of ordinary differential equations describing the time evolution of the variational parameters $a(t)$ and $b(t)$:

$$\dot{a}(t) = -2\psi_0^2\big[3G_2\,a(t)^2 + a(t)\big(2G_2\psi_0^2 + G_1\big)\big]\sin b(t) \tag{15}$$

and

$$\begin{aligned} \dot{b}(t) = -2\psi_0^2\big[&6a(t)G_2 + 2G_2\psi_0^2 + G_1\big]\cos b(t) \\ &- 5a(t)^2G_2 - \big(18G_2\psi_0^2 + 3G_1\big)a(t) + 12P_2k^2q^2 \\ &- 2P_1q^2 + 2P_2q^4 - 2G_1\psi_0^2 - 4G_2\psi_0^4. \end{aligned} \tag{16}$$

Let us remark that the above dynamical system admits steady states, and an interesting one is $(\bar{a},\bar{b})$, with

$$\bar{a} = 0, \quad \bar{b} = \arccos\left(-1 + \frac{P_2q^4 + 6P_2k^2q^2 - P_1q^2}{G_1\psi_0^2 + 2G_2\psi_0^4}\right). \tag{17}$$

Obviously, such fixed points exist only when we have $0 \leqslant q^2(P_2q^2 + 6P_2k^2 - P_1)/(G_1\psi_0^2 + 2G_2\psi_0^4) \leqslant 2$.

The TDVA has allowed obtaining the ordinary differential equations that describe the temporal dynamics of modulational perturbation $a(t)$. As we will show in the following section, the perturbation features the behavior of a classical oscillator, which evolves in a highly anharmonic effective potential.

B. Effective potential and instability criteria

From the set of differential equations derived in the above section, it is possible to determine the instability criteria of the lattice. As we are going to see later, the results from the time-dependent variational approach include not only the sought instability condition, but also and importantly an effective potential, unlike the familiar linear stability analysis. The expression of the effective Lagrangian (13) is such that $a(t)$ may be interpreted as the generalized coordinate of the system, while $b(t)$ gives the corresponding momentum. That is indeed what motivated our choice of the variant of ansatz in Eq. (12). The full Hamiltonian of the system is expressed as

$$H = -L + \int_{-\infty}^{\infty}\frac{\mathrm{i}}{2}\left(\frac{\partial\psi}{\partial t}\psi^* - \frac{\partial\psi^*}{\partial t}\psi\right)dx. \tag{18}$$

Using the integration limits imposed by the annular geometry, we get the full Hamiltonian of the system to be

$$\begin{aligned} H = \pi\big[&\tfrac{5}{3}G_2a^3 + \tfrac{3}{2}a^2\big(G_1 + 6G_2\psi_0^2 + 4G_2\psi_0^2\cos b\big) \\ &+ 2a\big(G_1\psi_0^2\cos b + 2G_2\psi_0^4\cos b - P_2k^4 + 2G_1\psi_0^2 \\ &+ 3G_2\psi_0^4 - P_2q^4 - 6P_2k^2q^2 + P_1q^2 + P_1k^2\big) \\ &+ G_1\psi_0^4 + \tfrac{2}{3}G_2\psi_0^6 + 2P_1k^2\psi_0^2 - 2P_2k^4\psi_0^2\big]. \end{aligned} \tag{19}$$

However, we can realize that $a(t)$ and $b(t)$ are canonically conjugate with respect to an effective Hamiltonian H_{eff} (i.e., $\frac{\partial a}{\partial t} = +\frac{\partial H_{\mathrm{eff}}}{\partial b}$ and $\frac{\partial b}{\partial t} = -\frac{\partial H_{\mathrm{eff}}}{\partial a}$) which reads

$$\begin{aligned} H_{\mathrm{eff}}(a,b) = &\tfrac{5}{3}G_2a^3 + \tfrac{3}{2}a^2\big(G_1 + 6G_2\psi_0^2 + 4G_2\psi_0^2\cos b\big) \\ &+ 2a\big(G_1\psi_0^2\cos b + 2G_2\psi_0^4\cos b + G_1\psi_0^2 \\ &+ 2G_2\psi_0^4 - P_2q^4 - 6P_2k^2q^2 + P_1q^2\big) + H_0, \end{aligned} \tag{20}$$

where $H_0 = G_1\psi_0^4 + \frac{2}{3}G_2\psi_0^6 + 2P_1k^2\psi_0^2 - 2P_2k^4\psi_0^2$. Let's remark in passing that $H = \pi(H_{\mathrm{eff}} + \Omega a)$. It should be noted that taking H_0 as any arbitrary constant does not qualitatively change the result. As this effective Hamiltonian has no explicit time dependence, it is an exact integral of motion on the subspace spanned by the ansatz (12). One may use $a(t=0) = 0$ without loss of generality; that yields $H_{\mathrm{eff}}(a(t=0),b(t=0)) = H_0$. Owing to the fact that the Hamiltonian is conserved, we have $H_{\mathrm{eff}}(a,b) = H_0 := 0$, and thus we can easily eliminate the generalized coordinate b between Eqs. (15) and (20). This leads to the following energy equation for the generalized coordinate a:

$$\tfrac{1}{2}\dot{a}^2 + V_{\mathrm{eff}} = 0, \tag{21}$$

where the effective potential is expressed as a sixth-order polynomial in a as

$$V_{\mathrm{eff}} = \alpha_6\,a^6 + \alpha_5\,a^5 + \alpha_4\,a^4 + \alpha_3\,a^3 + \alpha_2\,a^2. \tag{22}$$

The coefficients α_i read

$$\alpha_6 = \tfrac{25}{18}G_2^2, \quad \alpha_5 = \tfrac{5}{2}G_2\big(G_1 + 6G_2\psi_0^2\big),$$
$$\alpha_4 = -\tfrac{10}{3}G_2P_2\,q^4 + \tfrac{10}{3}G_2(P_1 - 6P_2k^2)q^2 + \tfrac{9}{8}G_1^2 + \tfrac{101}{6}G_1G_2\psi_0^2 + \tfrac{175}{6}G_2^2\psi_0^4,$$
$$\alpha_3 = 3\psi_0^2\big(G_1 + 2G_2\psi_0^2\big)^2 - 3P_2\big(G_1 + 6G_2\psi_0^2\big)q^4 + 3(P_1 - 6P_2k^2)\big(G_1 + 6G_2\psi_0^2\big)q^2,$$
$$\alpha_2 = 2P_2^2\,q^8 - 4P_2(P_1 - 6P_2k^2)q^6 + \big[2(P_1 - 6P_2k^2)^2 - 4P_2\psi_0^2\big(G_1 + 2G_2\psi_0^2\big)\big]q^4 + 4\psi_0^2(P_1 - 6P_2k^2)\big(G_1 + 2G_2\psi_0^2\big)q^2.$$

As we can see, the energy equation (21) describes a classical object located at position $a(t)$ at time t, and subjected to a highly anharmonic external potential V_{eff}. The effective potential in Eq. (22) depends on the key parameters of the system, including the dispersion parameters P_1 and P_2, the nonlinearity strengths G_1 and G_2, the background wave amplitude ψ_0 and wave number k, as well as the excitation wave number q and modulational perturbation a. Such a potential may thus provide a lot of information about the dynamical properties of the system. For instance, through the curvature of the potential at $a = 0$, we may determine the stability of the dynamics. When the potential is concave, the dynamics is unstable; when it is is convex, the dynamics is stable. The concavity of the potential here is given by its second-order derivative $\frac{\partial^2 V_{\text{eff}}}{\partial a^2}|_{a=0} = \alpha_2$. Such a mathematical evidence allows finding the dynamical instability criteria of the system. Hence the dynamics is expected to be unstable when α_2 is negative. Thus the condition for the instability to occur is

$$P_2^2\,q^4(q^2 + 6k^2)^2 - 2P_2q^2(q^2 + 6k^2)\big(P_1q^2 + G_1\psi_0^2 + 2G_2\psi_0^4\big) + P_1q^2\big(P_1q^2 + 2G_1\psi_0^2 + 4G_2\psi_0^4\big) < 0. \tag{23}$$

In what follows, the parameter $G = G_1 + 2G_2\psi_0^2$ that carries information on both the cubic and quintic nonlinearities denotes the so-called effective nonlinearity. Equation (23) is a criterion that determines the occurrence of dynamical instability in anharmonic lattices with fourth-order dispersion (FOD) and cubic-quintic nonlinearities. Using that condition, we can get a lot of information on the dynamical behavior of the system with respect to its internal properties and the external perturbation.

For instance, the relation (23) provides us with the various instability regions. In the P_1-P_2 plane, as plotted in Fig. 1, we display the instability domains for $G < 0$, i.e., focusing effective nonlinearity [in the left panel (a)], and for $G > 0$, i.e., defocusing effective nonlinearity [in the right panel (b)]. The light regions depict unstable modes and the dark regions depict stable ones. We used without loss of generality $G_1 = -1, G_2 = -0.5$ in the left panel (a), and $G_1 = +1, G_2 = +0.5$ in the right panel (b). In both panels (a) and (b), we considered $\psi_0 = 1.0$ and $k = 0$ (motionless background). In order to determine the stability of points in that plot, the excitation wave numbers q were taken in the range $[0, 16\pi]$. It appears that for $G < 0$, unstable modes are expected to excite for both normal

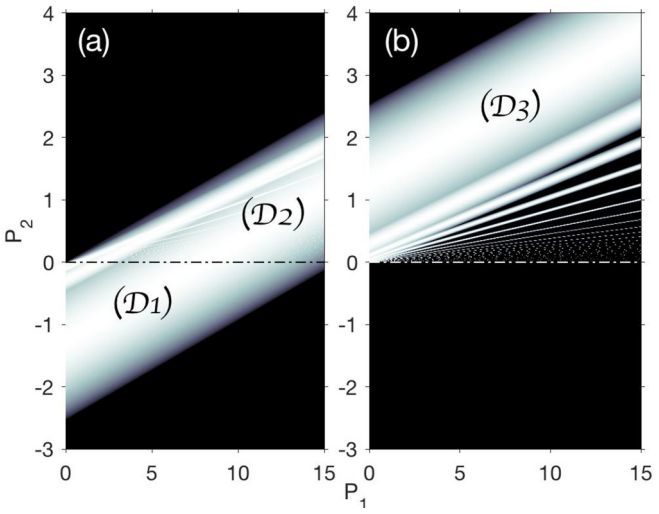

FIG. 1. Instability domains in the P_1-P_2 plane for $G < 0$ (a), and for $G > 0$ (b), i.e., focusing and defocusing effective nonlinearity, respectively. The light and dark regions depict unstable and stable modes, respectively. We distinguish three main unstable domains, denoted by $(\mathcal{D}1)$, $(\mathcal{D}2)$, and $(\mathcal{D}3)$.

[33] (negative P_2) and anomalous (positive P_2) FOD. The unstable domain, consisting of $(\mathcal{D}1)$ and $(\mathcal{D}2)$, is bounded by two straight lines, $P_2 = \lambda_0 P_1$ and $P_2 = \lambda_0 P_1 + \lambda_1$, with $\lambda_0 = 1/(q^2 + 6k^2)$ and $\lambda_1 = 2\lambda_0 G\psi_0^2/q^2$. Meanwhile for $G > 0$, only positive values of the FOD parameter may excite unstable modes. In this case, the unstable domain, denoted by $(\mathcal{D}3)$, contains a wide marginal region which separates it from the bottom stable domain. It is depicted by white stripes and lines, on a black background, converging towards the origin. That region may contain both stable and unstable modes. It should be noted that while the FOD parameter can be either positive or negative for anharmonic atomic lattices, it can be positive only for a BH lattice.

From the above relation (23), we can also obtain the local growth rate of instability; it is given by the relation

$$\text{Gain} = q^2(q^2 + 6k^2)\left\{2\left(-P_2 + \frac{P_1}{q^2 + 6k^2}\right) \times \left[P_2 - \frac{P_1q^2 + 2G_1\psi_0^2 + 4G_2\psi_0^4}{q^2(q^2 + 6k^2)}\right]\right\}^{1/2}. \tag{24}$$

In Fig. 2 we display the instability gains in the P_1-P_2 plane for $G < 0$ (a), and for $G > 0$ (b). The gain grows parabolically from the boundary line $P_2 = \lambda_0 P_1 + \lambda_1$ and abruptly drops close to the boundary line $P_2 = \lambda_0 P_1$. It is constant along any line $P_2 = \lambda_0 P_1 + \text{const}$ belonging to the unstable domain. It is easy to show that the gain in the above Eq. (24) coincides with the gain obtained in Ref. [29] where the propagation of extremely short pulses in optical fiber was investigated. Our result in Eq. (23) clearly reproduces already known particular cases. For instance, when there is no FOD ($P_2 = 0$), we readily get $P_1q^2(P_1q^2 + 2G_1\psi_0^2 + 4G_2\psi_0^4) < 0$ as previously obtained in the study of modulational instability of optical fibers [34], and of Bose-Einstein condensates [31,35]. When both the FOD and the quintic nonlinearities are absent ($G_2 = P_2 = 0$), the condition reads $P_1q^2(P_1q^2 + 2G_1\psi_0^2) < 0$ as

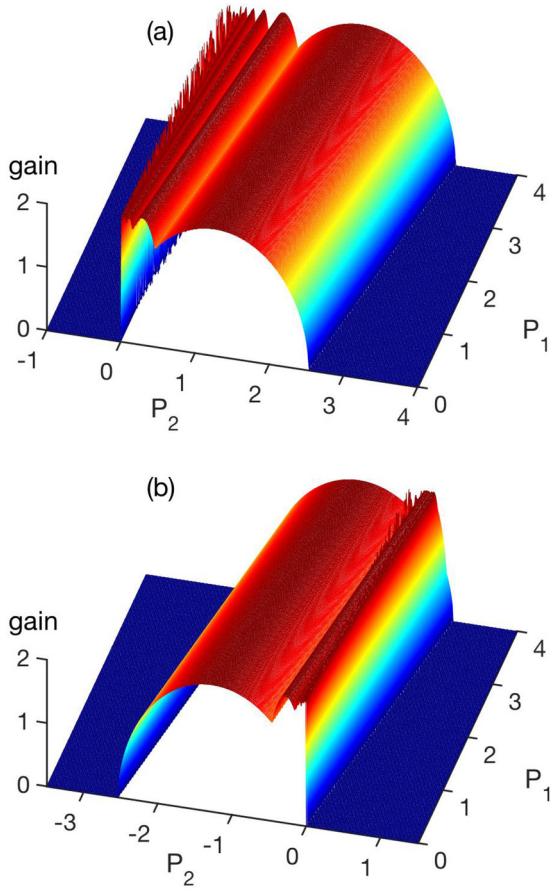

FIG. 2. Instability gains in the P_1-P_2 plane when the effective nonlinearity parameter G is (a) negative and (b) positive.

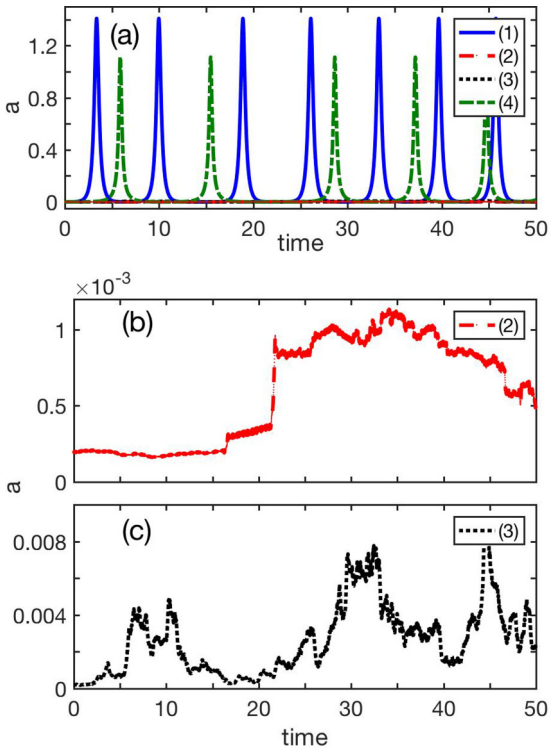

FIG. 3. Time evolution of the modulational perturbation a (predicted by the TDVA) when the FOD parameter $P_2 < 0$. The different modes are (1) $G_1 = -1.0, G_2 = -0.25, q = 1$; (2) $G_1 = -1.0, G_2 = -0.25, q = 3$; (3) $G_1 = -1.0, G_2 = -0.25, q = 6$; (4) $G_1 = +1.0, G_2 = -1.05, q = 1$. We used $P_2 = -1.0$. The modes are all taken in the instability domain ($\mathcal{D}1$). In panel (a), we readily see that the two modes (1) and (4) are unstable as they show high peaks, while the modes (2) and (3) seem stable. A zoom of the evolution displayed in the panels (b) and (c) clearly shows that they are not stable too.

previously found by Rapti *et al.* [36]. In what follows, we mostly investigate the effects of quintic nonlinearity and FOD dispersion in the instability of the system.

C. Dynamics of the modulational perturbation

Unlike the linear stability analysis, the TDVA has given not only the instability criteria (23), but also the effective potential (22). More interestingly, it has also provided us with the couple of nonlinear ordinary differential equations (15) and (16) that describe the evolution of the modulational perturbation within the system. We solve it using the fourth-order Runge-Kutta numerical scheme. The time runs up to $t = 50$, and the initial values used are $b(t = 0) = 0$ and $a(t = 0) = 2.10^{-4}$, which is small enough compared to the unperturbed wave amplitude $\psi_0 = 1.0$. We distinguish two main cases, namely, when the FOD is normal or anomalous, i.e., the FOD parameter P_2 is negative or positive, respectively.

In Fig. 3 we present the time evolution of the modulational perturbation a according to the TDVA in the case where the FOD parameter P_2 is negative and for four different modes, which are

(1) $G_1 = -1, G_2 = -0.25, q = 1$ (blue solid line),
(2) $G_1 = -1, G_2 = -0.25, q = 3$ (red dashed line),
(3) $G_1 = -1, G_2 = -0.25, q = 6$ (black dotted line),
(4) $G_1 = +1, G_2 = -1.05, q = 1$ (green dash-dotted line).

The top panel readily shows that the two modes (1) and (4) are unstable as the perturbation neither remains constant nor performs mild oscillations around its initial value. Instead the perturbation grows exponentially until $a_{\max} = 1.4$, which is so many (more than 1000) times its initial value and exhibits instability peaks. Moreover, we realize that the perturbation shows for the modes (1) and (4) a regular periodic pattern with well-separated peaks that reminds one of the breathing or collapse and revival processes. Meanwhile the modes (2) and (3) seem stable in the top panel. This is actually not true, since a zoom of the evolution displayed in the middle and bottom panels clearly shows that there is a significant growth also in those modes, with smaller amplitudes. The amplitude erratically changes but eventually increases to values higher compared to the initial value. So all the modes (1)–(4) investigated are predicted to be unstable.

In the case where the FOD parameter P_2 is positive, Fig. 4 presents the time evolution of the modulational perturbation a, as predicted by the TDVA, for four different modes, which are

(I) $G_1 = -1, G_2 = -0.25, q = 1$ (blue solid line),
(II) $G_1 = -1, G_2 = -0.25, q = 3$ (red dashed line),
(III) $G_1 = -1, G_2 = -0.25, q = 6$ (black dotted line),

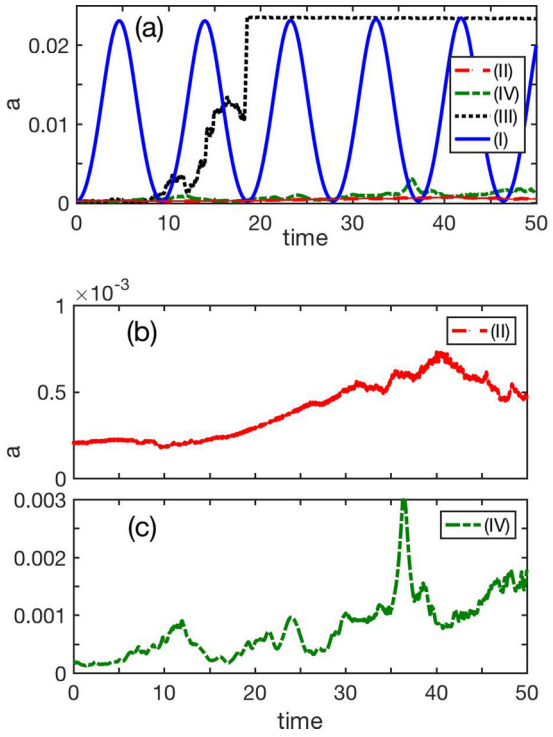

FIG. 4. Time evolution of the modulational perturbation a (predicted by the TDVA) when the FOD parameter $P_2 > 0$. The different modes are (I) $G_1 = -1.0, G_2 = -0.25, q = 1$; (II) $G_1 = -1.0, G_2 = -0.25, q = 3$; (III) $G_1 = -1.0, G_2 = -0.25, q = 6$; (IV) $G_1 = +1.0, G_2 = -0.75, q = 6$. We used $P_2 = +1.0$. All modes are taken in the instability domain ($\mathcal{D}2$). The modes depicted in panel (a) appear to be all unstable because a zoom of the evolution displayed in panels (b) and (c) clearly shows a significant growth in the modes with smaller amplitudes.

(IV) $G_1 = +1, G_2 = -0.75, q = 6$ (green dash-dotted line).

As displayed in Fig. 4, we can readily realize that all the modes are unstable, since the perturbation amplitude a grows away from its initial value. In particular, the perturbation shows a regular pattern for the mode (I), while it remains weaker for the modes (II) and (IV). In comparison to the previous case with negative P_2, we here have smaller growth rates, which nevertheless cause the perturbation amplitude to grow to values more than 100 times its introduced value. The various evolutions of the modulational perturbation show that whether the cubic nonlinearity parameter G_1 is positive or negative, the quintic parameter can be appropriately chosen or tuned in such a way that the systems qualitatively exhibits the same behavior.

IV. DIRECT NUMERICAL INVESTIGATIONS

The analytical findings obtained in Sec. III via TDVA predict that when the instability condition (23) is satisfied, a plane wave with wave number k modulated by a small-amplitude perturbation of wave number q undergoes modulation instability. As is well known, that phenomenon is characterized by self-induced modulation of the perturbation that may result in the subsequent generation of localized structures. In order to confirm our analytical predictions and generate the structures

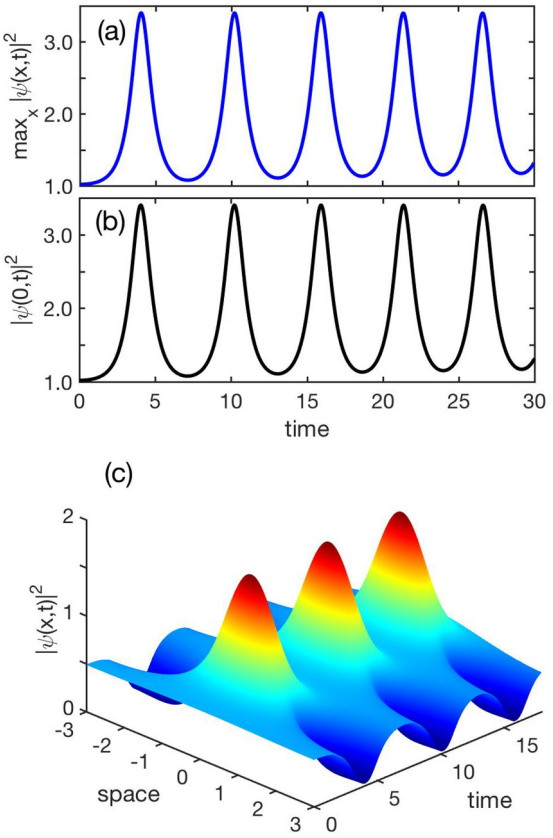

FIG. 5. Dynamics of the lattice in the case where $P_2 < 0$, depicted through (a) the time evolution of maximum amplitude of the wave in space $\max_x |\psi(x,t)|^2$, (b) the time evolution of the wave amplitude in the lattice center $|\psi(0,t)|^2$, and (c) the 3D spatio-temporal profile of a breather that forms in the system. We used $q = 1$, $G_1 = -1.0$, $G_2 = -0.25$, and $P_2 = -1.0$. The modes lie in the instability domain ($\mathcal{D}1$), and Akhmediev-like breathers are generated.

that form within the lattice, we employ direct numerical techniques based on the split step and fast Fourier transform (FFT) methods. The boundary condition are intrinsically assumed to be periodic due to the use of FFT. The initial condition used is $\psi(x,0) = \psi_0 e^{ikx}[1 + \varepsilon \cos(qx)]$, where $\varepsilon = 0.01$ is small compared to $\psi_0 = 1.0$. The wave number $k = 0$ (motionless background) and second-order dispersion parameter $P_1 = 1.0$ everywhere they are not explicitly given. The computations are run for $-x_m \leqslant x \leqslant x_m = 2\pi$, with 2^{11} spatial grid points.

A. Pattern formation in the case of normal FOD

Consider the case where the FOD parameter P_2 is negative. The modes considered in this section lie in the instability domain ($\mathcal{D}1$), i.e., the (white) instability domain analytically obtained and displayed in Fig. 1 [panel (a) only]. Direct numerical computations show that the instability onset results in the creation of periodic structures in the system. As shown in Fig. 5, there is formation of quasistable localized breathing structures in the lattice. Panel (a) presents the time evolution of the maximum of the square amplitude, $\max_x |\psi(x,t)|^2$. Panel (b) portrays the square amplitude, $|\psi(0,t)|^2$, taken at the lattice center $x = 0$ as time evolves. Both the maximum square amplitude and the central square amplitude periodically

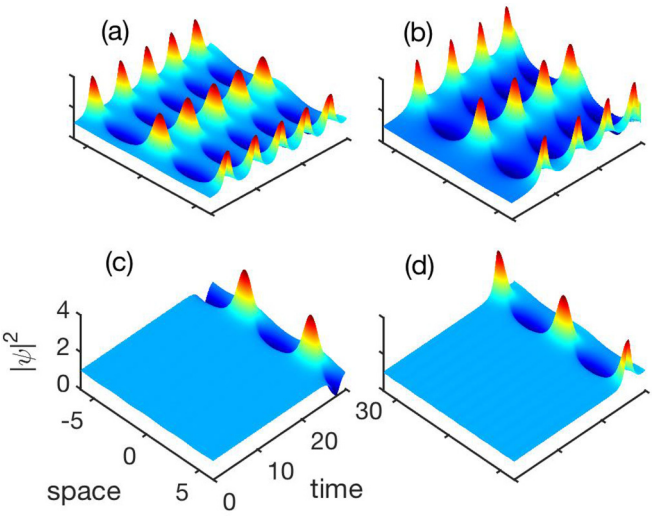

FIG. 6. Dynamics of the lattice in the case where $P_2 < 0$, depicted through the spatio-temporal profile $|\psi(x,t)|^2$ of localized structures that form in the system, for the modes (a) $q = 1, G_1 = -1, G_2 = -0.25$; (b) $q = 1, G_1 = +1, G_2 = -1.05$; (c) $q = 2, G_1 = -1, G_2 = -0.25$; and (d) $q = 3, G_1 = -1, G_2 = -0.25$. We used $P_2 = -1.0$. The modes lie in the instability domain ($\mathcal{D}1$), and Akhmediev-like breathers are generated.

exhibit growth up to a maximum value, close to 3.4, followed by a decay. Such a breathing character reminds one of the Akhmediev breather [37–39] as well as the collapse and revival phenomenon [40,41] known in many nonlinear systems. The profile of the breather that forms is displayed in panel (c). The pattern formation onset time as well as the breathing period and the pulse amplitude depend on the system's and perturbation's parameters. Figure 6 displays the nonlinear wave patterns induced in the system by various unstable modes (a) $q = 1, G_1 = -1, G_2 = -0.25$; (b) $q = 1, G_1 = +1, G_2 = -1.05$; (c) $q = 2, G_1 = -1, G_2 = -0.25$; and (d) $q = 3, G_1 = -1, G_2 = -0.25$. Comparing the patterns in panels (a) and (b), we readily realize that the pulses form whether the cubic nonlinearity parameter G_1 is positive or negative. The pulse height, pattern onset time, and time separation between pulses increase when the effective nonlinearity strength G is reduced from -1.50 to -1.10. Comparing the patterns in panels (a), (c), and (d), it emerges that the wave number affects the pattern onset time. The pattern appears later for higher wave numbers. As is well known, we observe that the pulses form at lattice positions $x = 2n\pi$, with $n = 0, \pm 1, \pm 2, \ldots$, for odd wave numbers. For even wave numbers, they form at lattice positions $x = 2(n+1)\pi$, with $n = 0, \pm 1, \pm 2, \ldots$. It should be noticed that the modes (a), (b), (c), and (d) correspond to the modes (1), (4), (2), and (3), respectively, considered in Sec. III C for analytical investigations. Even though the modes (c) and (2) differ by the wave numbers, the behavior of the system in this case is qualitatively the same as both wave numbers are even. Indeed, we realized that the modes with $G_1 = -1, G_2 = -025$ and $q = 2,4,6$ produce patterns similar to (c), while the ones with $G_1 = -1, G_2 = -025$ and $q = 3,5,7$ produce patterns similar to (d).

We can therefore compare the direct numerical results in Fig. 6 with the corresponding analytical ones in Fig. 3. It emerges that for the modes in Figs. 6(a) and 6(b), breathers form, and as soon as the numerical experiment begins, as predicted analytically in Fig. 3(a) through the modes (1) and (4). For the modes in Figs. 6(c) and 6(d), the breathers appear only later, which can be understood from the analytical results in terms of weaker amplitude growth as depicted in Figs. 3(b) and 3(c). Hence, the numerical results excellently agree with the analytical predictions in the case of normal higher-order dispersion.

B. Pattern formation in the case of anomalous FOD

Consider the case where the FOD parameter P_2 is positive, which corresponds to modes that lie in the instability domains ($\mathcal{D}2$) or ($\mathcal{D}3$) displayed in Fig. 1 (both left and right panels). As we present in this section, direct numerical computations show that the instability onset results in the creation of quasistable periodic structures in the system only for modes located in domain ($\mathcal{D}2$).

Indeed, as shown in Fig. 7, quasistable localized breathing structures are generated in the lattice. Figure 7(a) presents the maximum of the square amplitude, $\max_x |\psi(x,t)|^2$, taken along the lattice at each time. Figure 7(b) portrays the time evolution of the central square amplitude, $|\psi(0,t)|^2$. As in the case of normal FOD, both the maximum square amplitude and the central square amplitude periodically exhibit growth up to a maximum value, close to 2.0 here, followed by a decay. The square amplitude of the wave at $x = 0$ or at any arbitrary point shows, however, an additional behavior. The amplitude in the pulse rapidly oscillates around its initial value ψ_0, as known for solitonic chirped-like pulses [42,43]. Moreover, the phase of the wave as presented in Fig. 7(c) actually changes in the middle of each temporal blob or heap [44]. Such a pulsating character reminds of a pulsed laser in optics. The profile of the subsequent solitonic chirped-like pulses is displayed in panel (d). Unlike the case of normal FOD, the wave amplitude at a given time is the same everywhere in the lattice. Various modes picked from the instability domain ($\mathcal{D}2$) may generate solitonic chirped-like pulses with same height (peak amplitude), but different width (pulse time duration), different peak-to-peak time (pulse time separation) and even different emission time (time of first peak appearance). Figure 8 presents the time evolution of the wave amplitude in the lattice center, $|\psi(0,t)|^2$, for the modes with different wave number $q = 3,5,6$. It is clear that the emission time and time duration (τ_p) of the chirped pulse change with the wave number q. Indeed, even though the chirped pulses generated for $q = 3$ and 6 seem to have the same duration, this is obviously not the case for $q = 5$. Besides, the chirped pulses for the modes $q = 3,5,6$ reach their peak value at different times $t = 24$, 12, and 8, respectively. The chirped pulse width τ_p also changes with the nonlinearity strengths. To examine in detail how the nonlinearity affects τ_p, we keep $q = 6$ and vary the parameters G_1 and G_2, within the instability domain ($\mathcal{D}2$), i.e., keeping $G < 0$. The results displayed in Fig. 9 for $G_1 = -1$ show that the chirped pulse broadens when we increase G_2 (from -1.50 to -0.75). We mention in passing that the second chirped pulse (blue curve with $G_2 = -0.25$) corresponds to the mode (III) that has been analytically investigated in Sec. III C, and the predicted dynamics has been portrayed in Fig. 4 (black dotted

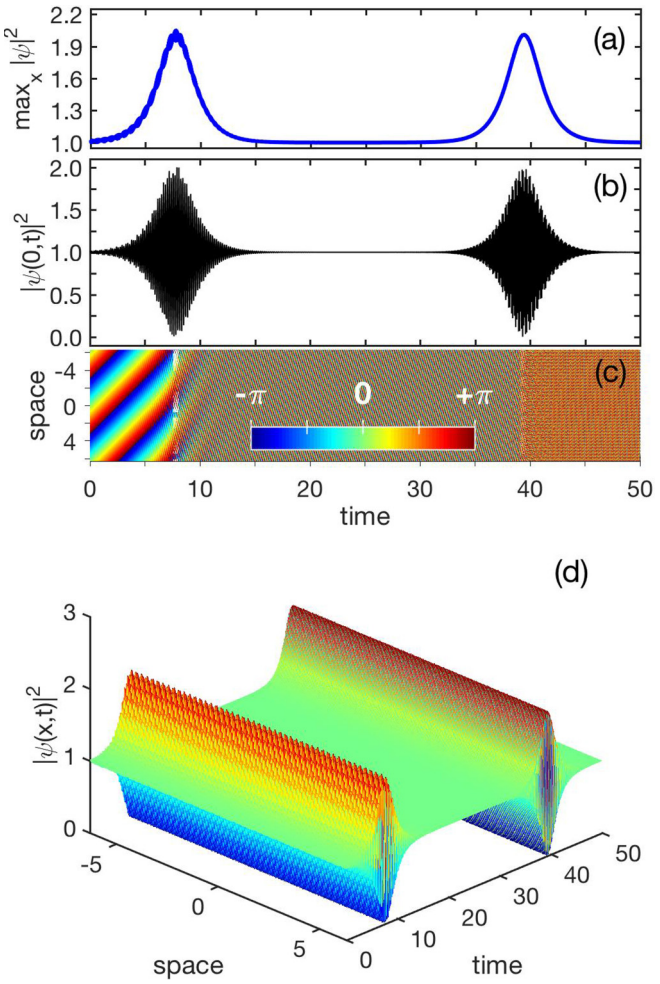

FIG. 7. Dynamics of the lattice in the case where $P_2 > 0$, depicted through (a) the time evolution of maximum amplitude of the wave in space $\max_x|\psi(x,t)|^2$, (b) the time evolution of the wave amplitude in the lattice center $|\psi(0,t)|^2$, (c) the spatio-temporal evolution of the wave phase, and (d) the 3D profile of solitonic chirped-like pulses that form in the system. We used $k = 1.0$, $q = 6$, $G_1 = -1.0$, $G_2 = -0.25$, and $P_2 = 1.0$. The modes lie in the instability domain ($\mathcal{D}2$). Let us note in passing that for $k = 0$, we obtain a kind of hybrid structure composed of breather-like pulses embedded within chirped-like pulses.

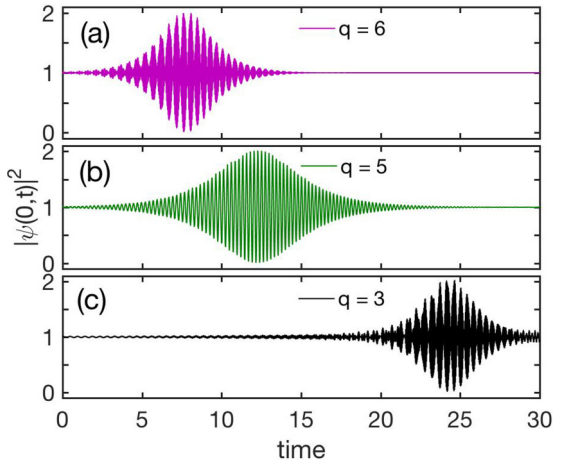

FIG. 8. Dynamics of the lattice in the case where $P_2 > 0$, depicted through the time evolution of the wave amplitude in the lattice center $|\psi(0,t)|^2$ for (a) $q = 6$, (b) $q = 5$, (c) $q = 3$ (chirped-like pulses from top to bottom). We used $k = 1.0$, $G_1 = -1.0$, $G_2 = -0.25$, and $P_2 = 1.0$. The modes lie in the instability domain ($\mathcal{D}2$).

line). The mode generates quasistable localized patterns as predicted, showing a good agreement between direct numerical simulations and the TDVA. Similar results as in Fig. 9 are obtained for $G_1 = +1$. As displayed in Fig. 10, it shows that the chirped pulse broadens when we increase G_2 (from -0.50 to $+0.25$). Hence the chirped pulse width τ_p increases with G_2 (provided that $G < 0$). We have obtained similar results for the peak-to-peak time.

We define the pulse (time) duration to be the timescale τ_p such that the maximum amplitude over a pulse centered at time τ_e can be fitted as $\max_x|\psi(x,t)|^2 := \psi_0^2[1 + \mathrm{sech}^2(\frac{t-\tau_e}{\tau_p})]$, where τ_e is any time when the pulse amplitude reaches its peak value. It appears that the pulse duration increases when the magnitude of (focusing) effective nonlinearity becomes smaller. For instance, taking $q = 6$, $P_2 = +1$, $G_1 = +1$, and $G_2 = -1.5, -1.25, -1.0, -0.75$ (i.e., $G = -2.0, -1.5, -1.0, -0.5$), we obtain $\tau_p \approx 1.7, 2.2, 3.3, 6.5$, respectively. Besides, we noticed that when we rescale the time span with respect to τ_p in each of the four plots, the resultant plots merge. This strongly infers that there really exists a timescale in the dynamics of the lattice. Moreover, the pulses displayed in both Figs. 9 and 10 with same color are qualitatively and even quantitatively similar. Indeed, despite the fact that the corresponding G_1 and G_2 are different, computing the corresponding G give equal values, which are $G = -2.0, -1.5, -1.0, -0.5$ (for pulses from the left to the right). Thus, the effective nonlinearity with strength $G = G_1 + 2G_2\psi_0^2$ better determines the dynamics of the system than the cubic and quintic nonlinearities taken separately. Reducing the magnitude $|G|$ of the focusing effective nonlinearity

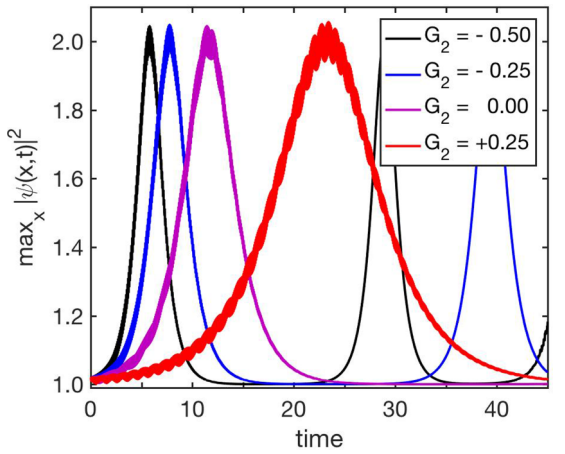

FIG. 9. Dynamics of the lattice in the case where $P_2 > 0$ and $G < 0$, with $G_1 < 0$, depicted through the time evolution of maximum amplitude of the wave in space $\max_x|\psi(x,t)|^2$ until the appearance of the first pulse, for $G_2 = -0.50, -0.25, 0.00, +0.25$ (pulses from left to right). We used $k = 1.0$, $q = 6$, $G_1 = -1.0$, and $P_2 = 1.0$. The modes lie in the instability domain ($\mathcal{D}2$).

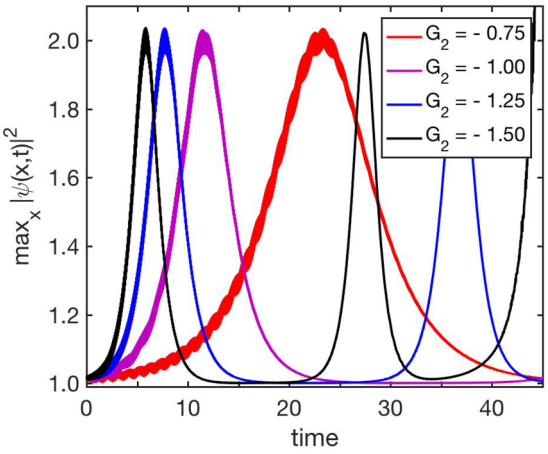

FIG. 10. Dynamics of the lattice in the case where $P_2 > 0$ and $G < 0$, with $G_1 > 0$, depicted through the time evolution of maximum amplitude of the wave in space $\max_x|\psi(x,t)|^2$ until the appearance of the first pulse, for $G_2 = -1.50, -1.25, -1.00, -0.75$ (pulses from left to right). We used $k = 1.0$, $q = 6$, $G_1 = +1.0$, and $P_2 = 1.0$. The modes lie in the instability domain ($\mathcal{D}2$).

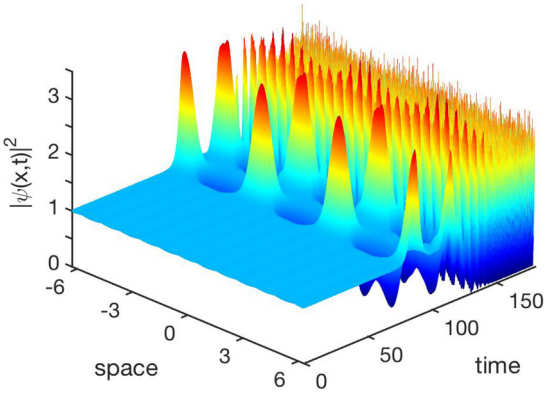

FIG. 11. Dynamics of the lattice for a mode picked in the instability domain ($\mathcal{D}3$) depicted through the spatio-temporal profile $|\psi(x,t)|^2$ of the wave. We used $q = 3$, $P_2 = 0.5 > 0$, $G_2 = -0.25$ and $G_1 = +1$ (satisfying $G > 0$).

increases the pulse time duration. Hence exciting the dynamical instability in modes depicted in the instability domain ($\mathcal{D}2$) generates solitonic chirped-like pulses, with time duration that changes with the perturbation wave number and increases with the effective nonlinearity strength, over some timescale. The formation of solitonic chirped-like pulses may be due to compensation between the negative kinetic energy due to FOD and the positive energies due to the second-order dispersion and the cubic-quintic nonlinearities. Chirped pulses generated can then be interpreted in terms of Rabi oscillations that happen on top of the background wave amplitude. Such oscillations were proposed as a signature of the quantumness of the system [45]. Therefore, the instability domain ($\mathcal{D}2$) provides a regime where the quantum nature of the lattice at small amplitudes is clearly resolved.

As far as modes located in domain ($\mathcal{D}3$) are concerned (they satisfy $P_2 > 0$ and $G > 0$), the system is dynamically stable for a given time. Then the instability sets on and various localized structures, including standard breathers and modulated breathers, may shortly appear. However, they quickly collapse and a strong exponential growth of the wave amplitude gives rise to an unstable structure without well-localized patterns. An example of such a wave profile is provided in Fig. 11. We can see that localized pulses appear, but disappear after a short time.

Hence, modulated waves with modes depicted in the instability domains ($\mathcal{D}1$) and ($\mathcal{D}2$) develop into Akhmediev-like breathers and solitonic chirped-like pulses, respectively. Meanwhile, modulated waves with modes depicted in the instability domain ($\mathcal{D}3$) always eventually grow exponentially and exhibit nonsolitonic patterns.

C. Dynamics of the lattice in the particular case $P_2 = 2\omega P_1$

The above results are general and apply for any arbitrary couple of dispersion coefficients (P_1, P_2). In this section, we consider the particular case when $P_2 = 2\omega P_1$, i.e., P_2 has the same sign as P_1 (which is positive). Taking into account the fact that $P_1 = 1$ for most computations in this work, the positive values of P_2 are nothing but twice ω. Given that P_2 in Eq. (5) has been rescaled in units of 24ω, the particular case $P_2 = 2\omega P_1$ simply amounts to $P_2 = P_1/12$, which obviously depicts a straight line in the instability domains ($\mathcal{D}2$) or ($\mathcal{D}3$) when G is negative or positive, respectively, as shown in Fig. 1. The slope of the straight line is small compared to λ_0, and then the modes depicted in the instability domain ($\mathcal{D}3$) happen to lie only at its bottom part, which is a marginal region. Such modes may then suffer from instability or not, depending on the value of P_2.

In view of the fact that P_2 and P_1 are both positive in Sec. IV B, the results obtained there may also be applied here. The remaining constraints in the lattice dynamics are mostly about the nonlinearity strengths and wave phase. Besides, we have $K = 0$ (near the lower gap edge) from Eq. (3). Then the displacement of the nth atom for low amplitude oscillations reads

$$\theta(x,t) \equiv \mathrm{Re}[\psi(x,t)e^{-i\omega t}], \tag{25}$$

where $x = n\varepsilon$ and $\omega = \sqrt{2}\omega_0/2\sigma$. Hence the characteristic parameters of the lattice dynamics ω, G_1, and G_2 depend on two free parameters ω_0 and σ. Additionally, choosing G_1 implies that σ and ω_0 are related through $\omega_0 = 8G_1\sigma^4/(2\sigma^2 - 3)$, for $\sigma \neq \sqrt{3/2} \equiv \sigma_0$. Obviously, the case $\sigma = \sigma_0$ just trivially imposes $G_1 = 0$, which is of no interest in this work. Then we get

$$\omega = \frac{2\sqrt{2}G_1\sigma^3}{\sigma^2 - \sigma_0^2}, \quad G_2 = \frac{17G_1}{24}\frac{(\sigma^2 - \sigma_-^2)(\sigma^2 - \sigma_+^2)}{\sigma^2(\sigma^2 - \sigma_0^2)}, \tag{26}$$

where $\sigma_\pm^2 = (30 \pm 3\sqrt{15})/17$. Due to the fact that the characteristic parameters ω and G_2 now depend only on one free parameter σ, positive and different from σ_0, it is possible to represent ω as a function of G_2, as shown in the parameter domain in Fig. 12. The modes depicted using the asterisks are the ones that have been investigated in Sec. IV B, while the ones depicted using the balls have not been considered. The evolution of the modes depicted by the four rightmost asterisks

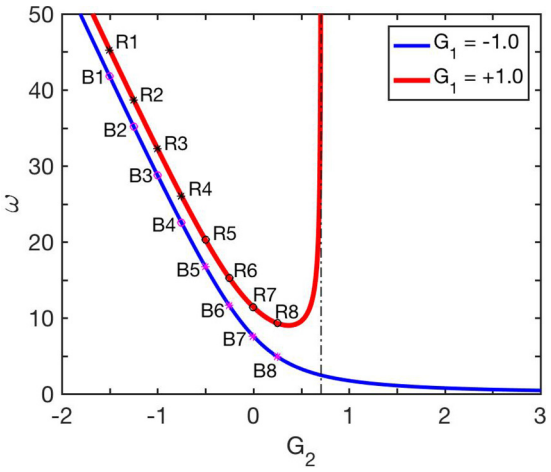

FIG. 12. Parameter domain in the particular case when $P_2 = 2\omega P_1$. The lines depict ω as a function of G_2 for $G_1 = +1$ [upper (red) curve] and $G_1 = -1$ [lower (blue) curve]. The dash-dotted line depicts the critical value $G_2 = 17/24$. On the horizontal axis, the modes Ri and Bi ($i = 1,\ldots,8$) correspond to $G_2 = -1.50,-1.25,-1.00,-0.75,-0.50,-0.25,0.0,0.25$. On the vertical axis, for the Ri (red line) we have $\omega \approx 45.26,38.68,32.25,26.05$ (asterisks) and 20.27,15.23,11.43,9.29 (balls). Meanwhile, for the Bi (blue line) we have $\omega \approx 41.78,35.20,28.75,22.54$ (balls) and 16.72,11.61,7.60,4.90 (asterisks). The modes depicted using the asterisks (R1, ..., R4 and B5, ..., B8) are the ones which have been investigated in Sec. IV B, with values of P_2 different from those in this section.

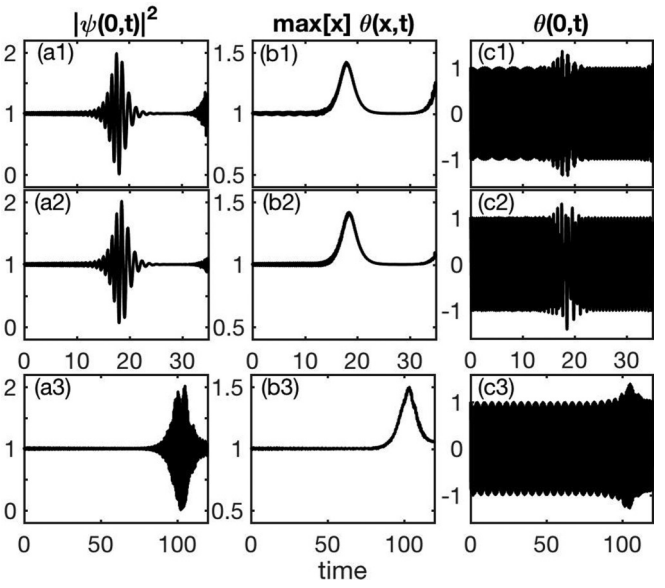

FIG. 13. Temporal profile of the wave in the lattice through $|\psi(x=0,t)|^2$, $\max_x\theta(x,t)$ and $\theta(x=0,t)$ in the special case when $P_2 = 2\omega P_1$. The top panels (a1), (b1), (c1) depict the dynamics of the mode R1 (located in the instability domain ($\mathcal{D}2$) with $G_1 = +1$), the middle panels (a2), (b2), (c2) depict the dynamics of the mode B5 [located in the instability domain ($\mathcal{D}2$) with $G_1 = -1$], and the bottom panels (a3), (b3), (c3) depict the dynamics of the mode R6 [located in the marginal region of the instability domain ($\mathcal{D}3$) with $G_1 = +1$]. The chirped pulse reaches its maximum amplitude at time $t_p \approx 17.97$, 18.46, and 102.6 for the modes R1, B5, and R6, respectively. The chirped pulse formation can be seen through both $\psi(x,t)$ and $\theta(x,t)$.

(modes B5, ..., B8 with $G_2 = -0.50, -0.25, 0.0, 0.25$) have been displayed in Fig. 9, for values of P_2 different than those in this section. Meanwhile, the evolution of the modes depicted by the four leftmost asterisks (modes R1, ..., R4 with $G_2 = -1.50, -1.25, -1.00, -0.75$) have been displayed in Fig. 10, for values of P_2 different than those in this section. The lines show possible values of ω as a function of G_2 for $G_1 = +1.0$ [upper (red) curve] and $G_1 = -1.0$ [lower (blue) curve]. For any mode with $P_1 = 1, P_2 = 1/12$ and given k,q, we must choose the set (G_2,ω) such that it is a point located in the top (red) curve or in the bottom (blue) curve for $G_1 = +1.0$ or -1.0, respectively. It emerges that the lattice allows no accessible value of ω for defocusing quintic nonlinearities stronger than the critical value $G_2 = 17/24$. Besides, when $G_2 \to 17/24$, the phase parameter ω is extremely sensitive to a change in G_2 for $G_1 = +1.0$. In the limit of higher strengths of focusing quintic nonlinearity, ω is a linear function of G_2 for both $G_1 = \pm 1.0$.

With these preliminaries, we can carry out simulations in order to get $\theta(x,t)$. The process consists in performing direct numerical computations to obtain the wave function $\psi(x,t)$. While running the simulations, at each space step and time step, the computed value of $\psi(x,t)$ is substituted into Eq. (25) to get the atomic displacement $\theta(x,t)$. We use $k = 1$ and $q = 6$ in line with the results presented in Sec. IV B.

In Fig. 13 we show the temporal profile of the wave in the lattice through the wave density $|\psi(x=0,t)|^2$ at the center, the maximum atomic displacement $\max_x\theta(x,t)$ over the lattice and the atomic displacement $\theta(x=0,t)$ at the lattice center. The top panels (a1), (b1), (c1) and the middle panels (a2), (b2), (c2) depict the dynamics of the modes R1 and B5, respectively, which are both located in the instability domain ($\mathcal{D}2$). As obtained in the above section with $P_2 = 1$, the propagation of unstable modulated waves lying in such a domain leads to the formation of solitonic chirped-like pulses in the lattice also for $P_2 = 1/12$, whether $G_1 = +1$ (as for R1) or $G_1 = -1$ (as for B5), provided that $G < 0$. The formation of chirped pulses is clearly seen not only in the wave amplitude $\psi(x,t)$ [see panels (a1), (a2), (a3)] from the eNLS equation (5), but also from the atomic displacement $\theta(x,t)$ [see panels (b1), (b2), (b3), (c1), (c2), (c3)] from the FK model in Eq. (1). Despite the difference in the nature of two-body interaction, the behavior of the wave is qualitatively the same. We obtained similar behaviors with the modes R1, ..., R4 and B1, ..., B8 all located in the instability domain ($\mathcal{D}2$). However, when the mode is located in the instability domain ($\mathcal{D}3$), the evolution of the wave as shown in the bottom panels (a3), (b3), and (c3) for the mode R6, is no more the same, which further validates the use of G as the effective nonlinearity strength. Indeed, comparing the timescale in the top and middle panels with that of the bottom panels, it appears that the chirped pulse forms and reaches its maximum amplitude at time $t_p \approx 17.97$, 18.46, and 102.6 for the modes R1, B5, and R6, respectively. Hence it readily emerges that the development of the instability lasts extremely longer in the latter case. Thus, to some extent, the mode R6 may be considered instead stable, which confirms that the marginal region of ($\mathcal{D}3$) has not only unstable modes, both also stable ones.

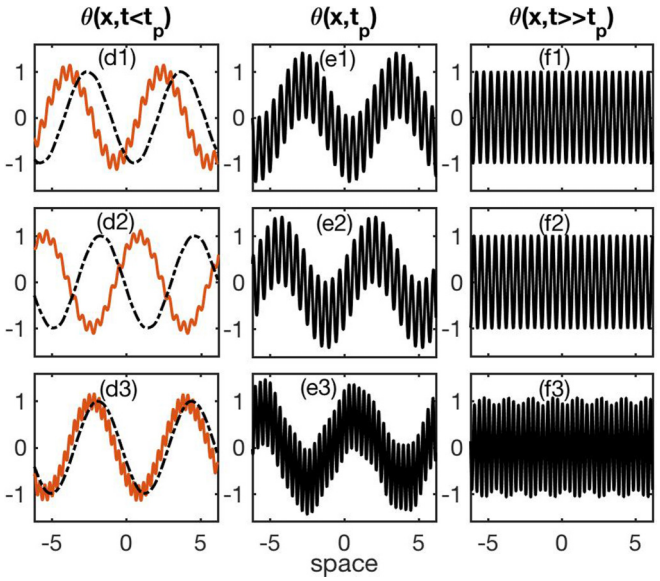

FIG. 14. Spatial profile of the wave in the lattice through $\theta(x,t < t_p)$, $\theta(x,t = t_p)$ and $\theta(x,t > t_p)$ in the special case when $P_2 = 2\omega P_1$, showing the wave-number amplification. The top panels (d1), (e1), (f1) depict the dynamics of the mode R1 (located in the instability domain ($\mathcal{D}2$) with $G_1 = +1$), the middle panels (d2), (e2), (f2) depict the dynamics of the mode B5 (located in the instability domain ($\mathcal{D}2$) with $G_1 = -1$), and the bottom panels (d3), (e3), (f3) depict the dynamics of the mode R6 (located in the marginal region of the instability domain ($\mathcal{D}3$) with $G_1 = +1$). In the left panels, the dashed and solid lines are the wave profiles outside and inside the chirped pulse, respectively. t_p is the time when the chirped pulse reaches its maximum amplitude. The formation of solitonic chirped-like pulses clearly modifies the wave in the lattice.

Those pieces of evidence, obtained from the temporal profiles, also appear in the spatial behavior of the wave, as portrayed in Fig. 14. It shows the spatial profile of the wave in the lattice through the atomic displacement θ before ($t < t_p$), during ($t = t_p$) and well after ($t \gg t_p$) the chirped pulse peak formation. The two profiles displayed before the peak formation in the three left panels [(d1), (d2), and (d3)] correspond to $t \ll t_p$ (dashed line) when no chirped pulse is forming, and $t \lesssim t_p$ (solid line) when the chirped pulse has started forming but has not yet reached its peak amplitude. The top, middle, and bottom panels correspond to the modes R1, B5, and R6, respectively, as in Fig. 13. As one can see, even though the spatial wave profile appears to be shifted for different modes, the form of the profiles is the same for the modes R1 and B5 before [panels (d1), (d2)], during [panels (e1), (e2)], and after [panels (f1), (f2)] the peak formation at time t_p, yet different for both modes. The shift of the profile is simply due to the phase shift at given times that we examined. However, it is clear that the generation of solitonic chirped-like pulses completely changes the wave in the lattice. While the wave shape and envelope are restored after the chirped pulse has collapsed, the wave number is drastically increased. In the case of the mode R6, likewise, the collapse of the chirped pulse equally leads to the amplification of the wave number, but the shape of the wave is not completely restored. The wave suffers from an additional modulation on top of the initial wave, which yields a modulated envelope.

Hence, despite the difference in the nature of two-body interaction, i.e., whether $G_1 = +1$ or -1, the behavior of the wave in the atomic lattice is qualitatively the same, as long as G_2 is taken in such a way that $G < 0$ while the modes lie in the same instability region. For modes taken in ($\mathcal{D}2$) or ($\mathcal{D}3$), solitonic chirped-like pulses are generated in the lattice. The signature of such a chirped pulse generation can be seen, not only in the eNLS derived from the FK and BH models, but also from the FK model itself, directly through both the temporal and the spatial profiles of the wave.

V. CONCLUDING REMARKS

In this work, we have analytically and numerically investigated the generation of localized patterns, through the dynamical instability process, in a chain of atoms that are coupled harmonically to their nearest neighbors, subjected to an external on-site potential and described by a modified Frankel-Kontorova model. In the limit of small-amplitude oscillations, the dynamics of such anharmonic lattices obeys an extended nonlinear Schrödinger equation with cubic-quintic nonlinearities and fourth-order dispersion. A similar equation has been derived from an extended Bose-Hubbard model with local three-body interactions in the limit of long wavelengths. Using the time-dependent variational approach, we have derived the equation of motion of the modulational perturbation. Through an effective potential affecting the dynamics of the perturbation, we have determined the instability-stability regions in the parameter domain as well as the instability gain. The time evolution of the modulational perturbation has been predicted in the interesting case when the lattice is unstable to perturbation. In order to confirm our analytical predictions, we have run direct numerical computations of the model equation, and a good agreement with the analytical results has been found. In the case when the effective nonlinearity satisfies the condition of instability, breather-like structures form in the lattice when the parameter of fourth-order dispersion is negative. Meanwhile when the parameter of fourth-order dispersion is positive, solitonic chirped-like pulses form, which reveals the quantum nature of the lattice at small oscillation amplitudes and long wavelengths. Such a chirped pulse formation can be seen through both the extended nonlinear Schrödinger equation and the FK model. Moreover, our results show that a timescale exists for the lattice and determine the formation of instability peaks. Due to the ubiquity of the model equation examined in this work, our results (on nonlinear atomic and bosonic lattices) may be used to understand the dynamics of modulated waves in many physical systems, including optical fibers, electrical transmission lines, DNA sequences, Bose-Einstein condensates, polaritons, and water waves.

ACKNOWLEDGMENTS

The authors are grateful to Axel Pelster and James Anglin for the constructive discussions that improved this work. E.W. acknowledges the Alexander von Humboldt foundation (Germany) for financial support through the AvH Postdoctoral Research Fellowship, and the Abdus Salam International Center for Theoretical Physics (Italy) for financial support through the Simon's Associateship program.

[1] H. A. Gersch and G. C. Knollman, Quantum cell model for bosons, Phys. Rev. **129**, 959 (1963).

[2] O. M. Braun and Y. S. Kivshar, *The Frenkel-Kontorova Model: Concepts, Methods, and Applications* (Springer-Verlag, Heidelberg, 2004).

[3] D. van Oosten, P. van der Straten, and H. T. C. Stoof, Mott insulators in an optical lattice with high filling factors, Phys. Rev. A **67**, 033606 (2003).

[4] I. Tikhonenkov, J. R. Anglin, and A. Vardi, Quantum dynamics of Bose-Hubbard Hamiltonians beyond the Hartree-Fock-Bogoliubov approximation: The Bogoliubov back-reaction approximation, Phys. Rev. A **75**, 033606 (2007).

[5] D. McKay, M. White, M. Pasienski, and B. De Marco, Phase-slip-induced dissipation in an atomic Bose-Hubbard system, Nature (London) **453**, 76 (2008).

[6] P. Schlagheck and D. L. Shepelyansky, Dynamical thermalization in Bose-Hubbard systems, Phys. Rev. E **93**, 012126 (2016).

[7] D. Jaksch and P. Zoller, The cold atom Hubbard toolbox, Ann. Phys. **315**, 52 (2005).

[8] T. Tomita, S. Nakajima, I. Danshita, Y. Takasu, and Y. Takahashi, Observation of the Mott insulator to superfluid crossover of a driven-dissipative Bose-Hubbard system, Sci. Adv. **3**, e1701513 (2017).

[9] F. Cosco, M. Borrelli, J. J. Mendoza-Arenas, F. Plastina, D. Jaksch, and S. Maniscalco, Bose-Hubbard lattice as a controllable environment for open quantum systems, Phys. Rev. A **97**, 040101 (2018).

[10] A. S. Tchakoutio Nguetcho and E. Wamba, Effects of nonlinearity and substrate's deformability on modulation instability in NKG equation, Commun. Nonlinear Sci. Numer. Simulat. **50**, 271 (2017).

[11] G. P. Agrawal, *Nonlinear Fiber Optics*, 4th ed. (Academic Press, Burlington, MA, 2007).

[12] Y. S. Kivshar and G. P. Agrawal, *Optical Solitons: From Fibers to Photonic Crystals* (Academic Press, San Diego, 2003).

[13] M. Toda, *Theory of Nonlinear Lattices*, 2nd ed., *Springer Series in Solid-State Sciences*, Vol. 20 (Springer-Verlag, Heidelberg, 1989).

[14] A. S. Tchakoutio Nguetcho, G. M. Nkeumaleu and J. M. Bilbault, Behavior of gap solitons in anharmonic lattices, Phys. Rev. E **96**, 022207 (2017).

[15] R. Chacón and P. J. Martínez, Controlling Chaotic Solitons in Frenkel-Kontorova Chains by Disordered Driving Forces, Phys. Rev. Lett. **98**, 224102 (2007).

[16] R. Asaoka, H. Tsuchiura, M. Yamashita, and Y. Toga, Density modulations associated with the dynamical instability in the Bose-Hubbard model, J. Phys. Soc. Jpn. **83**, 124001 (2014).

[17] R. Asaoka, H. Tsuchiura, M. Yamashita, and Y. Toga, Dynamical instability in the S = 1 Bose-Hubbard model, Phys. Rev. A **93**, 013628 (2016).

[18] O. Kimmoun, H. C. Hsu, B. Kibler, and A. Chabchoub, Nonconservative higher-order hydrodynamic modulation instability, Phys. Rev. E **96**, 022219 (2017).

[19] S. Trillo and S. Wabnitz, Dynamics of the nonlinear modulational instability in optical fibers, Opt. Lett. **16**, 986 (1991).

[20] P. J. Everitt, M. A. Sooriyabandara, M. Guasoni, P. B. Wigley, C. H. Wei, G. D. McDonald, K. S. Hardman, P. Manju, J. D. Close, C. C. N. Kuhn, S. S. Szigeti, Y. S. Kivshar, and N. P. Robins, Observation of a modulational instability in Bose-Einstein condensates, Phys. Rev. A **96**, 041601(R) (2017).

[21] S. Zhao, H. Yang, N. Chen, and C. Zhao, Controlled generation of high-intensity optical rogue waves by induced modulation instability, Sci. Rep. **7**, 39926 (2017).

[22] Till D. Kühner, Steven R. White, and H. Monien, One-dimensional Bose-Hubbard model with nearest-neighbor interaction, Phys. Rev. B **61**, 12474 (2000).

[23] S. Ejima, F. Lange, H. Fehske, F. Gebhard, and K. zu Münster, One-dimensional Bose-Hubbard model with local three-body interactions, Phys. Rev. A **88**, 063625 (2013).

[24] T. Sowiński, R. W. Chhajlany, O. Dutta, L. Tagliacozzo, and M. Lewenstein, Criticality in the Bose-Hubbard model with three-body repulsion, Phys. Rev. A **92**, 043615 (2015).

[25] H. Xu, W. Z. Chen, and Y. F. Zhu, Influence of the bond defect in driven Frenkel-Kontorova chains, Phys. Rev. B **75**, 224303 (2007).

[26] A. S. Tchakoutio Nguetcho, J. Li, and J. M. Bilbault, Bifurcations of phase portraits of a singular nonlinear equation of the second class, Commun. Nonlinear Sci. Numer. Simulat. **19**, 2590 (2014).

[27] M. Remoissenet, *Waves Called Solitons*, 3rd ed. (Springer-Verlag, Berlin, 2003).

[28] M. Peyrard and T. Dauxois, *Physique Des Solitons* (EDP Sciences/CNRS Edition, Paris, 2004).

[29] W. P. Hong, Modulational instability of optical waves in the high dispersive cubic-quintic nonlinear Schrödinger equation, Opt. Comm. **213**, 173 (2002).

[30] A. Tsurui, Wave modulations in anharmonic lattices, Prog. Theor. Phys. **48**, 1196 (1972).

[31] E. Wamba, A. Mohamadou, and T. C. Kofané, A variational approach to the modulational instability of a Bose-Einstein condensate in a parabolic trap, J. Phys. B **41**, 225403 (2008).

[32] S. Sabari, R. V. J. Raja, K. Porsezian, and P. Muruganandam, Stability of trapless Bose-Einstein condensates with two- and three-body interactions, J. Phys. B **43**, 125302 (2010).

[33] R. Paschotta, Chromatic dispersion, in *Encyclopedia of Laser Physics and Technology* (Wiley-VCH, Berlin, 2008).

[34] F.-II Ndzana, A. Mohamadou, and T. C. Kofané, Modulational instability in the cubic-quintic nonlinear Schrödinger equation through the variational approach, Opt. Comm. **275**, 421 (2007).

[35] E. Wamba, A. Mohamadou, and T. C. Kofané, Modulational instability of a trapped Bose-Einstein condensate with two- and three-body interactions, Phys. Rev. E **77**, 046216 (2008).

[36] Z. Rapti, P. G. Kevrekidis, A. Smerzi, and A. R. Bishop, Variational approach to the modulational instability, Phys. Rev. E **69**, 017601 (2004).

[37] B. Kibler, J. Fatome, C. Finot, G. Millot, F. Dias, G. Genty, A. Akhmediev and J. Dudely, The Peregrine soliton in nonlinear fibre optics, Nature Phys. **6**, 790 (2010).

[38] B. Kibler, J. Fatome, C. Finot, G. Millot, G. Genty, B. Wetzel, A. Akhmediev, F. Dias and J. Dudely, Observation of Kuznetsov-Ma soliton dynamics in optical fibre, Sci. Rep. **2**, 463 (2012).

[39] S. A. Chin, O. A. Ashour, and M. R. Belić, Anatomy of the Akhmediev breather: Cascading instability, first formation time, and Fermi-Pasta-Ulam recurrence, Phys. Rev. E **92**, 063202 (2015).

[40] E. M. Wright and P. Meystre, Collapse and revival in the micromaser, Opt. Lett. **14**, 177 (1989).

[41] M. Greiner, O. Mandel, T. W. Hänsch, and I. Bloch, Collapse and revival of the matter wave field of a Bose-Einstein condensate, Nature (London) **419**, 51 (2002).

[42] G. P. Agrawal, *Applications of Nonlinear Fiber Optics* (Academic Press, San Diego, 2001).

[43] P. L. Kelley, I. P. Kaminow, and G. P. Agrawal, (eds.), *Nonlinear Fiber Optics*, 3rd ed. (Academic Press, San Diego, 2001).

[44] H. Ebata and M. Sano, Model of heap formation in vibrated gravitational suspensions, Phys. Rev. E **92**, 053016 (2015).

[45] M. O. Scully and M. S. Zubairy, *Quantum Optics* (Cambridge University Press, Cambridge, 1997).